Monthly Notices
of the
ROYAL ASTRONOMICAL SOCIETY

MNRAS **459,** 4389–4396 (2016)
Advance Access publication 2016 April 21

doi:10.1093/mnras/stw933

Imprints of a high-velocity wind on the soft X-ray spectrum of PG1211+143

K. A. Pounds,[1]★ A. Lobban,[1] J. N. Reeves,[2] S. Vaughan[1] and M. Costa[2]

[1]*Department of Physics and Astronomy, University of Leicester, Leicester LE1 7RH, UK*
[2]*School of Physical Sciences, Keele University, Keele ST5 5BG, UK*

Accepted 2016 April 18. Received 2016 April 18; in original form 2015 October 5

ABSTRACT

An extended *XMM–Newton* observation of the luminous narrow-line Seyfert galaxy PG1211+143 in 2014 has revealed a more complex high-velocity wind, with components distinguished in velocity, ionization level, and column density. Here we report soft X-ray emission and absorption features from the ionized outflow, finding counterparts of both high-velocity components, $v \sim 0.129$c and $v \sim 0.066$c, recently identified in the highly ionized Fe K absorption spectrum. The lower ionization of the comoving soft X-ray absorbers imply a distribution of higher density clouds embedded in the main outflow, while much higher column densities for the same flow component in the hard X-ray spectra suggest differing sightlines to the continuum X-ray source.

Key words: galaxies: active – galaxies: individual: PG1211+143 – galaxies: Seyfert – X-rays: galaxies.

1 INTRODUCTION

The narrow-line Seyfert galaxy PG1211+143 is widely associated with ultra-fast, highly ionized outflows (UFOs), since the first detection in a non-BAL (broad absorption line) AGN (active galactic nucleus) of strongly blueshifted absorption lines of highly ionized gas, corresponding to a sub-relativistic outflow velocity of 0.15 ± 0.01c (Pounds et al. 2003; Pounds & Page 2006). Archival data from *XMM–Newton* and *Suzaku* have since shown similar UFOs are relatively common in nearby, luminous AGN (Tombesi et al. 2010, 2011; Gofford et al. 2013).

The frequency of these detections confirms a substantial covering factor – and hence significant mass and momentum in such winds, with the potential to disrupt star formation in the host galaxy. That realization has led to the view (e.g. King 2003, 2010) that powerful AGN winds could explain the remarkable correlation of the supermassive black hole mass and the velocity dispersion of the host galaxy's stellar bulge in a wide range of galaxies, the so-called M–σ relation (Ferrarese & Merritt 2000; Gebhardt et al. 2000).

It is noteworthy that the great majority of UFO detections (defined in Tombesi et al. 2010 with an outflow velocity $v \geq 10000\,\mathrm{km\,s^{-1}}$; 0.03c) are based on blueshifted absorption lines being identified with resonance transitions in Fe XXV and XXVI ions. The high ionization state has made absorption features difficult to detect in the soft X-ray region covered by higher resolution grating spectrometers on *XMM–Newton* and *Chandra*. A recent exception came from a re-analysis of the 2001 Reflection Grating Spectrometer (RGS; den Herder et al. 2001) data of PG1211+143, where a wavelength-to-velocity transformation was used to combine Lyman α absorption lines of several lower mass ions, finding compelling evidence for a soft X-ray UFO, with a Doppler-corrected velocity $v \sim 0.076$c, a factor of ∼2 less than that for the highly ionized flow (Pounds 2014). That lower velocity was confirmation of a second ionized absorption component required in a partial covering analysis of the combined 2001, 2004 and 2007 *XMM–Newton* broad-band spectra of PG1211+143 (Pounds & Reeves 2009), where modelling of continuum curvature made the outflow velocity poorly constrained.

To further explore the velocity and ionization structure of the fast wind in PG1211+143, an extended *XMM–Newton* observation was carried out during seven spacecraft orbits between 2014 June 2 and July 9. On-target exposures for individual orbits ranged from ∼50 to ∼100 ks, with a total duration of ∼630 ks. Full details of the *XMM–Newton* observing log and data processing are given in Lobban et al. (2016), reporting the results of a detailed timing analysis.

Pounds et al. (2016, hereafter Paper 1) present an analysis of the hard X-ray spectrum, based on data from the pn camera (Strueder et al. 2001), revealing new spectral structure in Fe K absorption lines, and dual velocities ($v \sim 0.066$c and $v \sim 0.129$c) in the highly ionized wind. The present paper reports a corresponding analysis of the 2014 soft X-ray spectrum of PG1211+143 using data from the RGS.

We assume an AGN redshift of $z = 0.0809$ (Marziani et al. 1996). Spectral fitting is based on the XSPEC package (Arnaud 1996) and includes absorption due to the line-of-sight Galactic column of

★ E-mail: kap@le.ac.uk

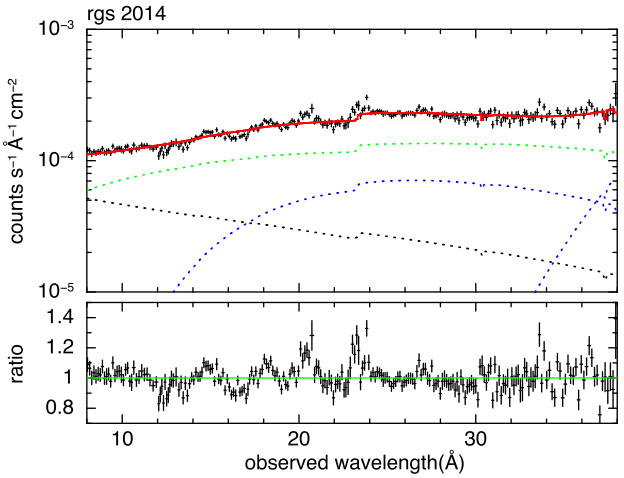

Figure 1. Continuum model consisting of hard ($\Gamma = 1.67$) and soft ($\Gamma = 2.9$) power-law components (black and green, respectively) taken from the higher energy spectral fit reported in Paper 1, with the addition of two blackbody components (blue) to match the 'soft excess'. The ratio of data to continuum illustrates the spectral structure imprinted on the X-ray continuum by photoionized absorption and emission from an outflowing wind.

$N_{\rm H} = 3\times10^{20}$cm^{-2} (Murphy et al. 1996; Willingale et al. 2013). 90 per cent confidence intervals on model parameters are based on $\Delta\chi^2 = 2.706$. Estimates for the black hole mass in PG1211+143 range from 3×10^7M$_\odot$ (Kaspi et al. 2000) to 1.5×10^8M$_\odot$ (Bentz et al. 2009), with the lower value making the historical mean luminosity close to Eddington. All quoted velocities are corrected for the relativistic Doppler effect.

2 SOFT X-RAY ABSORPTION AND EMISSION FROM CIRCUMNUCLEAR PHOTOIONIZED GAS

The composite 2014 RGS spectrum was produced by summing both RGS 1 and RGS 2 data over all seven *XMM–Newton* orbits with the SAS tool RGSCOMBINE, for a combined exposure of 1.27 Ms. For spectral modelling, the data were binned to a minimum of 25 counts per bin compatible with use of the χ^2 statistic, with the additional constraint that no bin be narrower than 1/3 of the mid-band full width at half-maximum resolution (Kaastra & Bleeker 2016).

Before attempting to model soft X-ray absorption and emission spectra we first fit the underlying soft X-ray continuum by extending the continuum model found in Paper 1, consisting of a hard and a soft power law, with the addition of a blackbody to match the soft excess. The soft power-law component was required in Paper 1 by inter-orbit difference spectra, represented over the 2–10 keV spectral band by an unabsorbed power law of photon index $\Gamma \sim 2.9$, and that continuum component was affirmed in the soft X-ray spectrum, finding inter-orbit difference spectra described by a power law of index $\Gamma \sim 2.8 \pm 0.1$. Such a steep continuum component has the potential to substantially dilute the imprint of photoionized gas on the overall soft X-ray spectrum and is included here in modelling spectral features in the 2014 RGS data.

Fig. 1 illustrates the resulting continuum model for the stacked RGS data over the full 8–38 Å waveband, with the corresponding data-model ratio indicating positive and negative residuals suggestive of significant absorption and emission from circumnuclear ionized gas. A measure of that spectral structure is given by the fit statistic χ^2_ν of 1251/721.

2.1 Spectral modelling from 12 to 30 Å with photoionized absorption and emission spectra

We begin spectral modelling over the 12–30 Å waveband where the data are of the highest statistical quality and the continuum fit gives a measure of spectral structure with χ^2_ν of 834/452. Publicly available photoionized grids computed for a power law $\Gamma = 2$ ionizing continuum[1] failed to fit strong Fe Unresolved Transition Array (UTA) absorption at ∼16–17 Å without an unrealistically high Fe abundance. Since absorption modelling can be highly sensitive to the form of the photoionizing continuum (e.g. see Reeves et al. 2013), we therefore generated a self-consistent set of multiplicative absorption and additive emission grids using the XSTAR v2.2 code (Kallman et al. 1996), with the spectral energy distribution (SED) of PG1211+143 based on concurrent data from the Optical Monitor (OM) (Mason et al. 2001) and EPIC-pn cameras, extrapolated from 1 to 1000 Rydberg. The SED, described in more detail in Lobban et al. (2016), is represented by a double-broken power law, where the OM data have been corrected for reddening [$E(B-V) = 0.035$].

The new XSTAR grids were computed in 10000 spectral bins between 0.1 and 20 keV, with an ionizing luminosity (1–1000 Ryd) of $3.8\times\ 10^{45}$ erg s^{-1} based on the SED fit, and over a range in ionization log ξ = 0–4 (where $\xi = L_{\rm ion}$/n r^2) and column density $N_{\rm H} = 10^{19}$–10^{22} cm^{-2}. Solar abundances were adopted for abundant elements (Grevesse & Sauval 1998), with additional grids computed for three- and five-fold overabundances of Fe. In each case grids were generated with turbulence velocities of σ = 300, 1000 and 3000 km s^{-1}, and for each multiplicative absorption grid (MTABLE) we generated a corresponding emission grid (ATABLE).

Absorption grids with a modest overabundance of Fe were found to give the best fit to the mean 2014 RGS spectrum, and the present analysis is based on a three-times-solar Fe abundance, with a turbulent velocity of 300 km s^{-1} for the absorber and 1000 and 3000 km s^{-1} for low- and high-ionization photoionized emission, respectively, to encompass velocity broadening. Free parameters in the absorption spectra are column density, ionization parameter, and outflow (or inflow) velocity in the AGN rest frame. For the emission spectra the column density is fixed at a suitably low value ($N_{\rm H} = 10^{20}$ cm^{-2}) to avoid significant opacity effects, with the ionization, flux level and velocity as free parameters.

The full XSPEC model is TBabs*((po1 + bbody)*mt + at + po2), where components 'mt' and 'at' represent the MTABLE and ATABLE grids of pre-computed photoionized absorption and emission spectra. Po2 represents the unabsorbed power law and TBabs the Galactic absorption. The absorbed power law has photon index ($\Gamma = 1.67$) tied to the value found in the pn analysis, with a single blackbody of kT∼0.1 keV completing the soft excess at 12–30 Å.

The addition of a single photoionized absorber greatly improved the 12–30 Å spectral fit (χ^2_ν of 681/451), for an ionization parameter log $\xi = 1.64 \pm 0.06$, absorption column density $N_{\rm H} = 5.0 \pm 0.6\times$ 10^{20} cm^{-2} and outflow velocity 0.061 ± 0.001c, close to the lower of the dual velocities reported in Paper 1. Adding a photoionized emission spectrum, with tied ionization parameter, produced a further substantial improvement to the fit (χ^2_ν of 601/449), with the linked ionization parameter increasing to log $\xi = 1.77 \pm 0.05$, and the absorber column falling slightly to $N_{\rm H} = 4.3 \pm 0.6\times$ 10^{20} cm^{-2}.

[1] ftp://legacy.gsfc.nasa.gov/software/plasma_codes/xstar.xspectables

Table 1. Parameters of the ionized outflow from 12 to 30 Å fit to the combined 2014 RGS data, with two photoionized absorbers, each defined by an ionization parameter ξ (erg cm s^{-1}), column density $N_{\rm H}$ (cm^{-2}), outflow velocity (in units of c) and absorbed luminosity (erg s^{-1}), and two photoionized emission spectra defined by the respective ionization parameter, outflow velocity, normalization and luminosity. Velocities are in the AGN rest frame and luminosities are in the fitted spectral band. The significance of each spectral component is measured by the increase in χ^2 when that component is removed and the spectrum re-fitted.

Component	logξ	$N_{\rm H}$ (10^{20})	$v_{\rm out}/c$	$L_{\rm abs/em}$	$\Delta\chi^2$
Absorber 1	1.35 ± 0.09	3.6 ± 0.7	0.061 ± 0.001	1.5×10^{42}	60/3
Absorber 2	1.8 ± 0.1	1.9 ± 0.5	0.077 ± 0.001	6×10^{41}	23/3
Emitter 1	1.1 ± 0.3	10	0.0016 ± 0.0005	6×10^{41}	59/3
Emitter 2	3.1 ± 0.3	10	0.001 ± 0.002	1.0×10^{42}	33/3

The absorber outflow velocity was unchanged, while the integrated emission spectrum had a much lower outflow velocity in the AGN rest frame.

The interaction of emission and absorption grids can be partly understood by the effects of self-absorption in resonance lines, while correctly modelling emission spectra also ensures a more accurate fit to the intrinsic continuum. Joint emission and absorption modelling also played a key role in analysis of the complex Fe K absorption spectrum reported in Paper 1, and underlines the importance of including both emission and absorption spectra in outflow studies of high-quality data.

The addition of a second ionized absorber gave a further substantial improvement to the 12–30 Å spectral fit (χ^2_ν of 569/446), with an ionization parameter log $\xi = 1.8 \pm 0.1$, absorption column density ($N_{\rm H} = 2.1 \pm 0.5\times 10^{20}$ cm^{-2}) and a significantly higher outflow velocity of 0.077 ± 0.001c. A second emission spectrum with tied ionization parameter yielded only a small further improvement in the spectral fit (χ^2_ν of 561/444).

Addition of the second absorber had the ancillary effect of reducing the ionization parameter of the first – lower velocity – absorber to log $\xi = 1.33 \pm 0.08$, with a further decrease in column density to $N_{\rm H} = 3.9 \pm 0.6\times 10^{20}$ cm^{-2}. While a second tied emission component had little effect, de-coupling the ionization parameters of both emission and absorption spectra did yield a further significant improvement in the fit (χ^2_ν of 534/442), with the emission components now covering a wider range of ionization. Table 1 summarizes the parameters of this best-fitting 12–30 Å model, including the luminosities added/extracted by the respective ionized emission/absorption spectra.

Fig. 2 illustrates different aspects of the 12–30 Å spectral fit. The top panel compares the data and final model, together with the three continuum components, unabsorbed power law (green), hard power law (dark blue) and blackbody (light blue). Absorption over most of the RGS waveband is seen to predominantly affect the blackbody emission component, representing the 'soft excess', a point which may be important in comparing the column density of similar flows measured in soft and hard X-ray spectra (see Section 6).

Strong absorption features include the Fe-M UTA at ∼16–17 Å (Behar, Sako & Kahn 2001), and resonance absorption in O VIII Lyman α and the OVII triplet observed at ∼19 Å and ∼22 Å, respectively. We find in Section 4 that the twin lines apparent in each resonance transition correspond to the distinct velocities found in the `xstar` modelling (Table 1). In turn, both low-velocity outflow components contribute to the strong Fe UTA, with a fit limited to the 14–18 Å waveband confirming both velocities are required (see also Appendix). We note this finding differs from that in the deep *Chandra* observation of NGC 3783, where (Holczer, Behar & Kaspi 2005) found the Fe M-shell absorber to be separated from the main outflow and essentially stationary.

The modelled photoionized emission spectra are highlighted in the mid-panel of Fig. 2, and directly compared with the stacked data in the lower panel, where the principal emission features are identified with resonance emission lines and radiative recombination continua (RRC) of the abundant H- and He-like ions of Ne, O, N and C. A more detailed comparison of data and model identifies a relative weakness of the modelled resonance emission in the triplet of OVII, suggesting a missing contribution from photoexcitation (Kinkhabwala et al. 2002) not included in the `xstar` grids. Adding a Gaussian emission line to the model described above finds a (blueshifted) line energy of 0.536 ± 0.002 keV (23.13 Å) and equivalent width 1.6 ± 0.4 eV, yielding an improvement in $\Delta\chi^2$ of 22/3.

In summary of Section 2, modelling of spectral structure in the 12–30 Å waveband finds strong evidence for absorption in a photoionized outflow, with velocity components ∼0.061c and ∼0.077c, which we assume are blended to match the lower of the dual velocities ($v \sim 0.066$c) identified in the primary highly ionized outflow in the (lower resolution) hard X-ray data (Paper 1).

From the model spectral fit we obtain an overall spectral luminosity in the 12–30 Å waveband of 5.73×10^{43} erg s^{-1}, with the low ionization absorbers together removing 2.1×10^{42} erg s^{-1}. The low ionization emission spectrum contributes a luminosity over the same waveband of 6×10^{41} erg s^{-1}, suggesting a covering factor of that flow component of ∼30 per cent. We return to considerations of the energy budget in Section 5.

3 EXTENDING THE RGS SPECTRAL FIT FROM 8 TO 38 Ú WAVEBAND

While the lower of the two outflow velocities ($v \sim 0.066$c) reported in Paper 1 may be clearly identified, the higher velocity ($v \sim 0.129$c) seen in the pn data is not detected. Since that difference might be due the faster flow being more highly ionized (as was found in the pn data of Paper 1), and the soft X-ray spectral model developed in Section 2 includes emission but not absorption from highly ionized outflow components, we now extend spectral modelling over the full 8–38 Å waveband shown in Fig. 1.

The more extended spectral fit confirms the two absorption components (absorber 1 and absorber 2) listed in Table 1, which are now included with only minor changes in the relevant parameters (abs 1 and abs 2) in Table 2. Significantly, the increased high energy coverage now also finds highly ionized counterparts of both high-velocity outflow components reported in Paper 1. Visual examination of the new spectral model confirms these new detections (abs 3 and abs 4 in Table 2) are largely due to several strong absorption lines of Fe XVIII – XX and resonance lines of Ne X and Mg XI observed in the 8–14 Å spectral region. The lower panels of Fig. 3 illustrate this point.

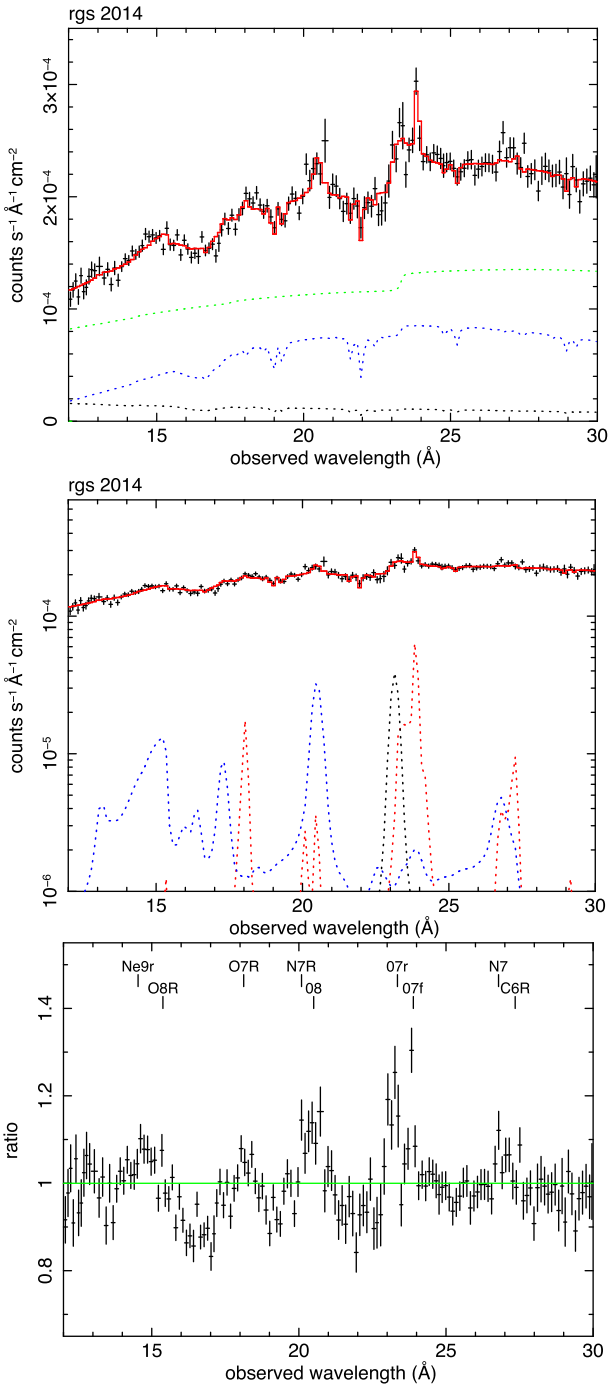

Figure 2. Top: a section of the mean soft X-ray spectrum of PG1211+143 from the stacked RGS data of the 2014 *XMM–Newton* observation, with photoionized absorption and emission added by XSTAR grids as described in the text. In the model the absorption affects only the hard power law (black) and blackbody (blue) continuum but not the steeper power law (green) identified in inter-orbit difference spectra. Mid panel: emission spectra from low (red) and high (blue) ionization components, with the parameters listed in Table 1. Lower: RGS data plotted as a ratio to the underlying continuum, with several discrete emission features identified with resonance emission lines and radiative recombination continua (R) of H- and He-like ions of Ne, O, N and C.

The extended model of the RGS soft X-ray spectrum now includes both low and highly ionized absorbers with velocities close to those identified in the hard X-ray spectrum reported in Paper 1. In addition to offering compelling support for both those primary (high column) outflow components, the higher resolution grating spectra provide an indication of additional fine structure in the lower velocity flow. Modelling the ionized emission with components of widely differing ionization parameter is a further measure of a complex flow.

A final search for additional absorption components to those noted above provides evidence for a still higher velocity outflow of 0.188 ± 0.001c (abs 5 in Table 2), given added weight as that velocity coincides closely with a marginal detection of a third highly ionized outflow component in the hard X-ray spectrum reported in Paper 1 (see also Appendix).

Based on the extended spectral fit, the observed spectral luminosity from 8 to 38 Å is 9.2×10^{43} erg s^{-1}, with absorption components 1 and 2, corresponding to the lower of the two velocities found in Paper 1, having removed 2.3×10^{42} erg s^{-1}, with components 3 and 4, associated with the more highly ionized outflow, removing 2.4×10^{42} erg s^{-1}. A lower ratio of emission-to-absorption for the highly ionized components may indicate a lower covering factor, or that much of the re-emission lies outside the RGS spectral band. We return to that question in Section 5.

Fig. 3 overlays the 2014 RGS data with the final spectral model. Comparison of the data-model residuals with those of Fig. 1 illustrates how the addition of the photoionized absorption and emission spectra detailed in Table 2 greatly improves the overall spectral fit.

4 IDENTIFYING INDIVIDUAL RESONANCE LINES

As noted earlier, the high ionization characteristic of powerful AGN winds renders much of that outflow transparent at soft X-ray energies, while the presence of an unabsorbed continuum component has a further diluting effect on observed soft X-ray absorption features. An added complexity in the soft X-ray spectrum of PG1211+143 is the dominance across parts of the RGS waveband of multiple transitions in Fe-L, including those partially screened by M-shell electrons (the Fe-M UTA; Behar et al. 2001). While the complexity of the Fe-L absorption can be accounted for reasonably well in spectral modelling, it is difficult to reliably identify individual transitions for use in measuring a blueshift.

Fortunately, the unusually deep *XMM–Newton* observation in 2014 has allowed the detection and identification of several absorption lines with physically resonance transitions in Ne, O, N and C (Fig. 4). Sequentially stepping through the stacked data with narrow Gaussians of width tied to the mid-band RGS resolution (∼30 mÅ) yields the observed absorption line wavelengths listed in Table 3, where each line identification provides a corresponding blueshift and outflow velocity. The 90 per cent confidence error on each wavelength was obtained using the `uncertainty` command for the relevant Gaussian parameter, which was then carried over to give the listed velocity uncertainty.

For the nine lines with $\Delta\chi^2$ of 5 or greater, two distinct velocity groups are found, with weighted mean outflows of $v\sim 0.060\pm 0.002$c and $v\sim 0.078\pm 0.002$c, in close agreement with the velocities of the two soft X-ray absorbers found in the XSTAR modelling. That agreement provides strong, independent support for those modelled outflow velocities, and correspondingly for the similar low-velocity component found in the primary, highly ionized outflow of PG1211+143 reported in Paper 1. The absence of

Table 2. Parameters of the ionized outflow of PG1211+143 over the full 8–38 Å waveband. Five photoionized absorbers are detected, each defined by an ionization parameter ξ (erg cm s^{-1}), column density $N_{\rm H}$ (cm^{-2}), outflow velocity (km s^{-1}) and absorbed luminosity (erg s^{-1}), with two photoionized emission spectra defined by the respective ionization parameter, outflow velocity, normalization and luminosity. Velocities are in the AGN rest frame and luminosities relate to the fitted spectral band.

Comp	logξ	$N_{\rm H}$ (10^{20})	$v_{\rm out}$/c	$L_{\rm abs/em}$	$\Delta\chi^2$
abs 1	1.5 ± 0.1	2.3 ± 0.4	0.061 ± 0.001	1.6×10^{42}	60/3
abs 2	1.9 ± 0.2	1.5 ± 0.5	0.077 ± 0.001	7×10^{41}	36/3
abs 3	3.0 ± 0.2	13 ± 6	0.131 ± 0.001	6×10^{41}	15/3
abs 4	3.2 ± 0.1	28 ± 15	0.061 ± 0.001	8×10^{41}	18/3
abs 5	2.5 ± 0.1	12 ± 5	0.188 ± 0.002	9×10^{41}	18/3
emit 1	1.7 ± 0.3	10	0.0012 ± 0.0006	9×10^{41}	73/3
emit 2	2.8 ± 0.6	10	0.002 ± 0.002	3×10^{41}	13/3

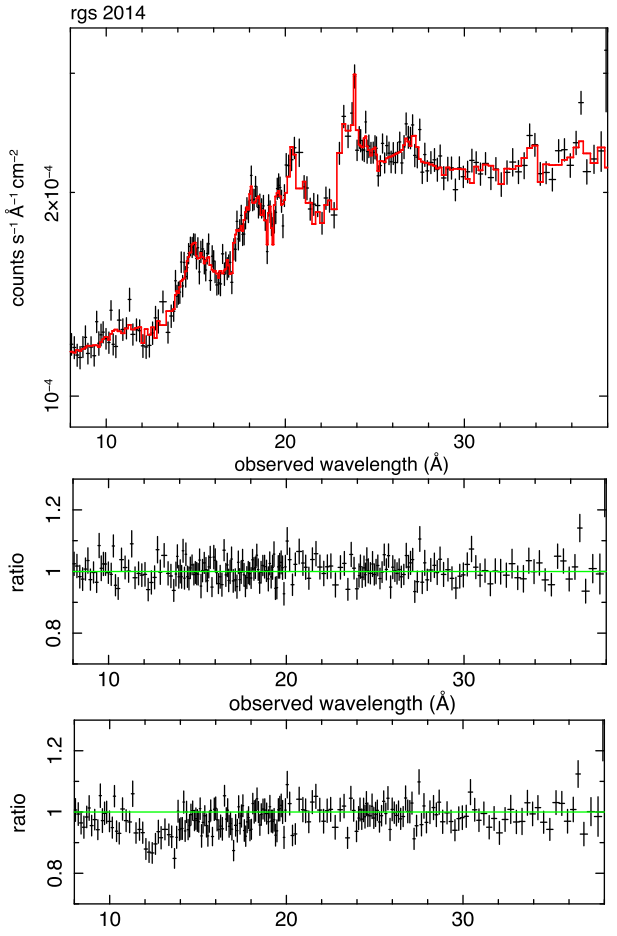

Figure 3. Top: the soft X-ray spectrum of PG1211+143, where fine structure on the soft X-ray continuum in Fig. 1 is successfully modelled by photoionized absorption and emission spectra from an outflowing wind with the parameters listed in Table 2. The middle panel shows the data-model residuals of this multi-component fit, where comparison with the lower panel – based on the restricted model of Table 1 - provides visual confirmation of the contributions of highly ionized components abs 3 and abs 4 in the extended 8–38 Å spectral fit.

identified absorption lines from the higher velocity outflow ($v \sim 0.13$c) may be understood from the relatively high ionization parameter of that component (abs 3 in Table 2), with the strongest absorption falling in the 12–14 Å waveband dominated by Fe-L transitions. This absorption complex is represented by a broad Gaussian in Fig. 4, where only two narrow lines are identified, both with Ne IX He-α. Interestingly, one narrow absorption line at ∼17 Å does stand out from the broad Gaussian fit to the Fe UTA and we see in the Appendix that this very likely corresponds to O VIII Lyα outflowing at the highest velocity component (abs 5) in Table 3.

5 COMPARING THE SOFT AND HARD X-RAY SPECTRAL MODELS

The above analysis has shown that the dual outflow velocities, of ∼0.129c and ∼0.066c, identified in highly ionized absorbing matter in the 2014 pn data (Paper 1) have comoving counterparts in the soft X-ray RGS spectra, with the higher spectral resolution of the grating spectra suggesting the lower velocity is actually a blend of two components.

As in Paper 1, simultaneous modelling of photoionized emission spectra is found to be important, both in determining the correct absorption parameters of the flow and in showing that a substantial fraction of the absorbed energy is returned via recombination and scattering from an extended outflow. To evaluate the energy budget of this re-processing requires extending the spectral bandwidth beyond that covered by the RGS, not least as the major part of the flow is absorbed only in the higher energy band covered by the EPIC cameras.

A direct comparison with the spectral model obtained from analysis of the simultaneous pn data in Paper 1 shows a good measure of agreement – and some important differences. To that end, the 2–10 keV spectral fit from Paper 1 was extended down to 0.4 keV to overlap the RGS spectrum. In making that extension the soft X-ray continuum was modelled by the addition of a blackbody component (kT∼0.1 keV), with soft X-ray absorption and emission requiring additional emission and absorption grids compared with Paper 1.

The extended 0.4–10 keV pn spectral fit remained remarkably good (χ^2_ν of 1783/1676), with the emission and absorption parameters listed in Table 4.

Comparison of the low ionization absorbers in Tables 2 and 4 tests the conjecture that abs 3 in Table 4 encompasses both abs 1 and abs 2 absorbers in the RGS spectra, with the velocity of $v \sim 0.066$c being a blend of two outflow components unresolved in the CCD data. Similar absorbed luminosities and column densities of the low ionization absorbers in the RGS and extended pn spectral models are now seen to support that view.

More surprising is the large difference in the column densities of highly ionized absorbers with the same velocity, but measured against the soft X-ray continuum (Table 2, abs 3 and abs 4) as compared with the hard X-ray spectrum (Table 4, abs 1 and abs

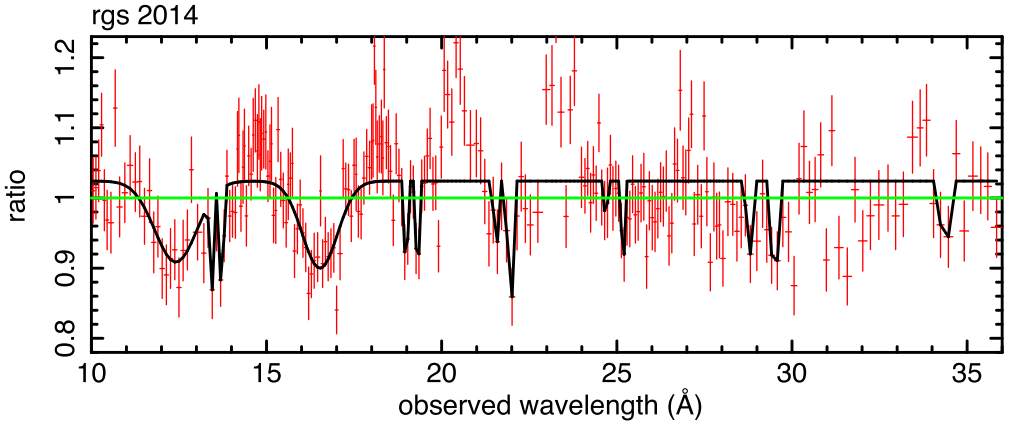

Figure 4. Gaussian line fitting to spectral structure in the stacked soft X-ray spectrum of PG1211+143 when the absorption and emission spectra defined in Table 2 have been removed from the model. A blind search reveals the 11 narrow absorption lines listed in Table 3, with 5 and 6 lines, respectively, found to match the two low ionization outflow velocities obtained from spectral modelling, when identified with principal resonance lines of Ne, O and N. Two broader Gaussians, at ∼12–13 Å and ∼16–17.5 Å, are used to fit a complex group of strong Fe-L lines and the Fe-M UTA, respectively.

Table 3. Observed wavelength of narrow Gaussians fitted to apparent absorption lines in the stacked 2014 RGS spectrum. 11 narrow lines are identified with six resonance transitions in Ne, O, N and C, with common blueshifts indicating two outflow velocities, both consistent with values obtained from spectral modelling.

Line	Lab (Å)	Obs (Å)	Rest (Å)	v_{out}/c	$\Delta\chi^2$
Ne9 He-α	13.447	13.41 ± 0.03	12.41 ± 0.03	0.080 ± 0.002	10/2
Ne9 He-α	13.447	13.73 ± 0.02	12.70 ± 0.02	0.057 ± 0.002	15/2
O8 L-α	18.968	18.99 ± 0.02	17.57 ± 0.03	0.077 ± 0.002	12/2
O8 L-α	18.968	19.31 ± 0.02	17.86 ± 0.03	0.060 ± 0.002	16/2
O7 He-α	21.602	21.54 ± 0.04	19.93 ± 0.03	0.080 ± 0.003	4/2
O7 He-α	21.602	21.94 ± 0.03	20.29 ± 0.03	0.062 ± 0.002	20/2
N7 L-α	24.781	24.69 ± 0.05	22.84 ± 0.03	0.080 ± 0.003	4/2
N7 L-α	24.781	25.17 ± 0.02	23.28 ± 0.03	0.062 ± 0.002	11/2
N6 He-α	28.787	28.75 ± 0.04	26.60 ± 0.03	0.078 ± 0.003	7/2
N6 He-α	28.787	29.50 ± 0.05	27.29 ± 0.03	0.054 ± 0.003	14/2
C6 L-α	33.736	34.35 ± 0.15	31.78 ± 0.03	0.060 ± 0.004	5/2

Table 4. Parameters of the ionized outflow from the previously published 2–10 keV spectral fit, extended down to 0.4 keV to overlap the soft X-ray spectrum covered by the RGS data. The continuum is modelled with absorption of a hard power law Γ ∼1.67 and blackbody (kT ∼0.1 keV), together with a softer unabsorbed power law of photon index Γ ∼2.9. Velocities are in the AGN rest frame and luminosities in the 0.4–10 kev spectral band.

Comp	logξ	N_H (10^{22})	v_{out}/c	$L_{abs/em}$	$\Delta\chi^2$
abs 1	3.95 ± 0.25	36 ± 24	0.129 ± 0.002	6×10^{41}	19/3
abs 2	3.50 ± 0.07	20 ± 9	0.066 ± 0.002	1.2×10^{42}	41/3
abs 3	1.7 ± 0.2	0.05 ± 0.02	0.066 (t)	1.4×10^{42}	24/3
emit 1	3.47 ± 0.05	1	0.007 ± 0.004	1×10^{42}	22/2
emit 2	1.46 ± 0.07	0.1	0.002 ± 0.002	1.3×10^{42}	15/2

2). In Section 6 we suggest an explanation in terms of different sightlines through the same outflow component, with potential to explore the X-ray source geometry.

An indication of the large covering factor of the outflow in PG1211+143 is now best measured from the broad-band 0.4–10 keV fit, where we find a total luminosity of 1.47×10^{44} erg s^{-1}, with the high and low ionization photoionized absorbers removing 1.8×10^{42} erg s^{-1} and 1.4×10^{42} erg s^{-1}, respectively, or ∼2.2 per cent of the spectral luminosity. In comparison, the high and low ionization emission spectra contribute luminosities over the same spectral band of 1×10^{42} erg s^{-1} and 1.3×10^{42} erg s^{-1}, respectively, with the total ionized emission indicating a time-averaged covering factor of ∼60 per cent.

6 DISCUSSION

An analysis of the soft X-ray spectrum of PG1211+143, produced by stacking RGS spectral data from all seven orbits of the 2014 *XMM–Newton* observation, has revealed both low and highly ionization outflow components comoving with each of the two primary high-velocity outflows detected in the hard X-ray spectrum (Paper 1). The higher resolution of the grating spectrometers reveals

additional velocity structure, with outflow velocities of 0.061 ± 0.002c and 0.077 ± 0.002c, apparently blended in the ∼0.066c component detected in the CCD spectra.

As in Paper 1 we find photoionized emission spectra are of similar significance to photoionized absorption in modifying the observed soft X-ray spectrum, with `xstar` modelling successfully reproducing most of the observed features, dominated by resonance emission lines and RRC of the abundant lighter metals (C, N, O, Ne) having K-shell energies covered by the RGS.

Extending the 2–10 keV spectral fit of Paper 1 down to 0.4 keV provides a direct comparison of the hard and soft X-ray analyses, allowing a quantitative measure of the impact of the photoionized outflow on the observed X-ray spectrum. From that assessment we find the outflow removes ∼2.3 per cent of the 0.4–10 keV spectral luminosity, with the ionized emission returning ∼80 per cent of that luminosity from scattering and recombination in an apparently extended outflow.

The relative column densities of comoving low and high ionization absorption components in Table 2 suggest an outflow in line of sight to the soft X-ray continuum source with a small filling factor of embedded higher density matter. Adopting that explanation, comparison of abs 1 and abs 4 (Table 2) shows a factor of ∼12 in column density and ∼50 in particle density, indicating a linear filling factor of ∼0.16 per cent. It appears that while such comoving absorbers may be readily understood in terms of higher density 'clouds' embedded in the main flow, perhaps caused by instabilities in the flow, the small filling factor implies a negligible contribution to the outflow mass rate and momentum.

Explaining the large difference in column density for flow components detected in the RGS and pn data *and having the same velocity and ionization parameter* is less straightforward. The highly ionized outflow components detected in the hard X-ray data (abs 1 and abs 2 in Table 4) have column densities ∼300 and ∼70 times larger than their soft X-ray counterparts (abs 3 and abs 4, respectively, in Table 2). We suggest an explanation might involve different lines-of-sight to the dominant hard and soft X-ray continuum sources (power law and blackbody in the model; Fig. 1).

For a conventional disc-corona geometry the intrinsic hard X-ray source would probably be confined to a smaller radius, closer to the black hole and – importantly – to the likely wind launch site (King & Pounds 2003), compared with the more extended thermal soft X-ray source in the inner accretion disc. For a sufficiently small launch radius, a diverging wind (King & Pounds 2015) might then explain the large difference in column density of the same flow component, observed in different sightlines to the hard and soft X-ray continuum sources. If confirmed, that possibility would offer the intriguing potential of using future observations of outflow spectra to explore the geometry of the X-ray continuum source in an AGN.

Finding multiple UFO velocities represents a new challenge to models of powerful AGN winds, not least to continuum-driving (King & Pounds 2003) which provides a natural mechanism for the highly ionized matter characteristic of UFOs, and has been found to provide a good match to their generic properties (King & Pounds 2015). We noted in Paper 1 that chaotic accretion (King & Pringle 2007), consisting of random prograde and retrograde events, could offer an explanation of a dual velocity wind, the two distinct outflow velocities relating to different orientations of the current inner accretion flow. With both flows close to Eddington, the prograde and retrograde discs would have different limiting values of the accretion efficiency η and hence of velocity (King & Pounds 2003). Confirmation here of a third outflow velocity, marginally detected in Paper 1, may indicate further complexity in the inner accretion flow, which remains the natural site for the launch of a high-speed, large-column wind. A further constraint is the relative variability in the primary (high-column) flow components over the *XMM–Newton* observations of 2001, 2007 and 2014, which will be reported in a future paper.

Meanwhile, in summary, the deep RGS exposure of PG1211+143 has provided an impressive demonstration of the application of high-resolution spectra in studying the properties of a classical UFO. However, while the imprint of overlying ionized gas on the soft X-ray spectrum provides detailed information on the dynamics of that outflow, with the soft X-ray absorption and emission being a high-resolution tracer of lower ionization matter entrained in the more massive highly ionized flows, it is important to note that the mass, momentum and mechanical energy rates of the UFO in PG1211+143 remain dominated by the much high column densities detected in the highly ionized (primary) flow components.

ACKNOWLEDGEMENTS

XMM–Newton is a space science mission developed and operated by the European Space Agency. We acknowledge in particular the excellent work of ESA staff at the European Space Astronomy Center in Madrid in successfully planning and conducting the relevant *XMM–Newton* observations. The UK Science and Technology Facilities Council funded the posts of AL and MC.

REFERENCES

Arnaud K. A., 1996, ASP Conf. Series Vol. 101, Astronomical Data Analysis Software and Systems, Astron. Soc. Pac., San Francisco, p. 17
Behar E., Sako M., Kahn S. M., 2001, ApJ, 563, 497
Bentz M. C., Peterson B. M., Pogge R. W., Vestergaard M., 2009, ApJ, 694, L166
den Herder J. W. et al., 2001, A&A, 365, L7
Ferrarese L., Merritt D., 2000, ApJ, 539, L9
Gebhardt K. et al., 2000, ApJ, 539, L13
Gofford J., Reeves J. N., Tombesi F., Braito V., Turner T. J., Miller L., Cappi M., 2013, MNRAS, 430, 60
Grevesse N., Sauval A. J., 1998, Space Sci. Rev., 85, 161
Holczer T., Behar E., Kaspi S., 2005, ApJ, 632, 788
Kaastra J., Bleeker J., 2016, A&A, 587, 151
Kallman T., Liedahl D., Osterheld A., Goldstein W., Kahn S., 1996, ApJ, 465, 994
Kaspi S., Smith P. S., Netzer H., Maoz D., Jannuzi B. T., Giveon U., 2000, ApJ, 533, 631
King A. R., 2003, ApJ, 596, L27
King A. R., 2010, MNRAS, 402, 1516
King A. R., Pounds K. A., 2003, MNRAS, 345, 657
King A. R., Pounds K. A., 2015, ARA&A, 53, 115
King A. R., Pringle J. E., 2007, MNRAS, 373, L90
Kinkhabwala A. et al., 2002, ApJ, 575, 746
Lobban A. P., Vaughan S., Pounds K. A., Reeves J. N., 2016, MNRAS, 457, 38
Marziani P., Sulentic J. W., Dultzin-Hacyan D., Clavani M., Moles M., 1996, ApJS, 104, 37
Mason K. O. et al., 2001, A&A, 365, L36
Murphy E. M., Lockman F. J., Laor A., Elvis M., 1996, ApJS, 105, 369
Pounds K. A., 2014, MNRAS, 437, 3221
Pounds K. A., Page K. L., 2006, MNRAS, 360, 1123
Pounds K. A., Reeves J. N., 2009, MNRAS, 397, 249
Pounds K. A., Reeves J. N., King A. R., Page K. L., O'Brien P. T., Turner M. J. L., 2003, MNRAS, 345, 705

Pounds K. A., Lobban A, Reeves J. N., Vaughan S., 2016, MNRAS, 457, 2951 (Paper 1)
Reeves J. N., Porquet D., Braito V., Gofford J., Nardini E., Turner T. J., Crenshaw D. M., Kraemer S. B., 2013, ApJ, 776, 99
Strueder L. et al., 2001, A&A, 365, L18
Tombesi F., Cappi M., Reeves J. N., Palumbo G. C., Yaqoob T., Braito V., Dadina M., 2010, ApJ, 742, 44
Tombesi F., Cappi M., Reeves J. N., Palumbo G. C., Braito V., Dadina M., 2011, A&A, 521, A57
Willingale R., Starling R. L. C., Beardmore A. P., Tanvir N. R., O'Brien P. T., 2013, MNRAS, 431, 394

APPENDIX A

We noted in Section 4 that it was difficult to identify the complex of Fe-L absorption lines at ∼11–14 Å and in the strong Fe-M UTA at ∼15.5–17 Å sufficiently reliably to allow a blueshift (and velocity) determination. That issue is made still more difficult when multiple velocities are involved, as illustrated in Fig. A1. There, the contributions of the $v \sim 0.061$c and $v \sim 0.077$c low ionization absorbers are shown separately, with the velocity difference resulting in a broader UTA than for a single velocity.

The upper panel of Fig. A1 also provides a direct confirmation of several individual line identifications, for example those at ∼19 Å and ∼19.3 Å identified with O VIII Lyα and associated with the above outflow velocities in Table 3. The lower panel of Fig. A1 shows the absorption profile for the highly ionized outflow component with $v \sim 0.188$c (Table 2, abs 5), where the same O VIII Lyα line is observed at ∼17 Å. While not fitted by a narrow Gaussian in Fig. 4, for the reasons noted above, a strong absorption line is clearly visible at that wavelength.

The important point to note is that while individual blueshifted line identifications are an important means of identifying an outflow – and a comoving line-set is better still – the most secure way to determine the parameters of any UFO is by spectral modelling, as described in Sections 2 and 3 for the present case of PG1211+143.

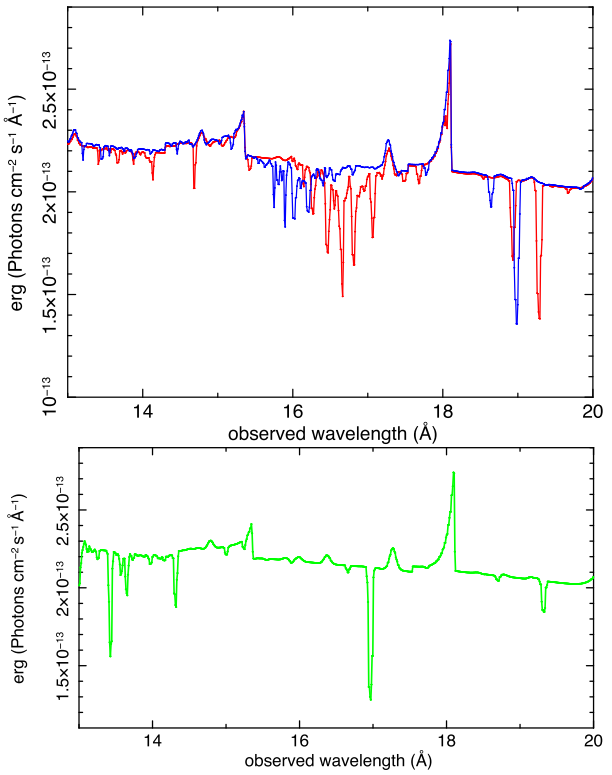

Figure A1. Top: photoionized absorption spectra of the two low-ionization components listed in Table 2 as abs 1 and abs 2, with outflow velocities of $v \sim 0.061$c (red) and $v \sim 0.077$c (blue). Lower: a similar plot for the more highly ionized absorber outflowing at $v \sim 0.188$c (green).

This paper has been typeset from a TEX/LATEX file prepared by the author.